

Giant Pulses of the Crab Nebula Pulsar as an Indicator of a Strong Electromagnetic Wave

M. V. Popov*, A. G. Rudnitskii**, and V. A. Soglasnov***

*Astro Space Center, Lebedev Physical Institute, Russian Academy of Sciences,
Profsoyuznaya ul. 84/32, Moscow, 117997 Russia*

Received May 20, 2016; in final form, September 12, 2016

Abstract—The spectra and visibility functions of giant pulses of the Crab Nebula pulsar derived from VLBI observations carried out through the “RadioAstron” project in 2015 are analyzed. Parameters of the scattering of the pulses in the interstellar medium are measured, namely, the scattering time and decorrelation bandwidth. A comparative analysis of the shapes of the spectra and visibility functions of giant pulses obtained in real observations and via modeling of their scattering is carried out. The results suggest the presence of short bursts ($dt < 30$ ns) in the structure of the giant pulses at 1668 MHz, whose brightness temperatures exceed 10^{38} K. These pulses propagate in the pulsar magnetosphere in a strong electromagnetic wave regime, leading to the generation of additional radiation perpendicular to the direction of propagation of the giant pulses. This radiation may be associated with anomalous components of the mean pulse profile observed at frequencies above 4 GHz.

DOI: 10.1134/S1063772917030064

1. INTRODUCTION

The radio emission of cosmic sources is distorted as it propagates through the interstellar medium. These distortions are caused by the dispersion of the radio waves and their scattering on inhomogeneities in the interstellar plasma. Due to the presence of free electrons in the interstellar medium, the group velocity of the radio waves is lower than the speed of light, and depend on frequency, such that the high-frequency component of the signal reaches the observer earlier than the low-frequency component. Such delays are not observed in the emission of continuum sources, but can be measured well for pulsar pulses, providing information about the electron density in the interstellar medium and its distribution in the Galaxy. These delays are the main basis of estimates of distances to pulsars [1]. Various methods have been developed to compensate for the influence of dispersion on the shapes of pulsar pulses [2].

The scattering of the radio waves, which is due to random bending of the beam as it passes through the inhomogeneity of the interstellar plasma, has several manifestations: an increase in the observed angular size of the source, an increase in the pulse duration, distortion of the radio spectrum with a characteristic frequency and time scale, and fluctuations of the

intensity (scintillation) in measurements with finite frequency bandwidths. All these manifestations of scattering have been intensely studied starting from the discovery of the first pulsars up to the current epoch, both theoretically and experimentally [5]. Theoretical studies have been based on models with a thin scattering screen located in the line of sight between the observer and the pulsar. This type of model was first introduced by Scheuer [3] and was subsequently developed by Rickett [4], Gwinn [6], and others.

The observed parameters of the scattering can be measured via the analysis of dynamical spectra, yielding the characteristic scintillation time scale and decorrelation bandwidth. The scattering angle can be directly measured only using Very Long Baseline Interferometry (VLBI) [7]. New opportunities in this area are offered by the “RadioAstron” space-ground interferometer [8], which enables measurements at 92 and 18 cm with angular resolutions of 1 milliarcsecond (mas) and 0.2 mas, respectively. RadioAstron observations have been used to measure the angular sizes of the scattering disks of the five pulsars B0329+54 [9], B1641-45, B1749-28, B1933+16 [10], and B0531+21 [11]. In our current study, we consider the measurement of scattering parameters based on RadioAstron VLBI observations of giant pulses of the Crab Nebula pulsar B0531+21 carried out in 2015.

*E-mail: mwpopov@gmail.com

**E-mail: almax1024@gmail.com

***E-mail: vsoglasn@asc.rssi.ru

2. SOME PROPERTIES OF GIANT PULSES OF THE CRAB NEBULA PULSAR B0531+21

The main property of giant pulses, which also led to their name, is their high intensities, reaching peak radio flux densities of millions of Jy [12, 13]. The energy distribution of these pulses is a power law, $N(E) \propto E^\gamma$, with power-law indices from -1.5 to -3.5 in various frequency ranges [14, 15]. At 1668 MHz—the frequency at which the observations analyzed here were made—roughly five to ten pulses a minute with peak flux densities exceeding 4000 Jy were recorded. Several pulses with flux densities exceeding 10^5 Jy were recorded each hour. These high flux densities make it possible to analyze individual interferometric correlation functions (visibility functions) with high signal-to-noise ratios. Thus, interferometric observations of these giant pulses can yield instantaneous amplitudes and phases of the visibility function.

The integration time is determined by the duration of a giant pulse, and very short pulse durations are their second characteristic property. A summary of measurements of the characteristic durations of giant pulses from the Crab Nebular pulsar B0531+21 is given by Hankins et al. [15]. It follows from these data that the duration of the giant pulses at decimeter wavelengths is mainly determined by scattering, with their duration at 1668 MHz being about $10 \mu\text{s}$. The intrinsic duration measured at frequencies above 5 GHz is about $1 \mu\text{s}$. It is important to know the fine structure of the giant pulses for our subsequent analysis. Regular pulses of ordinary pulsars consist of one or several subpulses with durations of tens or hundreds of microseconds (μs). It was shown earlier that the internal structure of these subpulses corresponds to white noise. This model has become known as the Amplitude Modulated Noise model [16]. In turn, the internal structure of giant pulses studied at high frequencies (from 6 to 46 GHz) with sub-nanosecond resolution [15, 17] often displays strong, isolated peaks with durations of less than 0.2 ns and with peak flux densities of millions of Jy. These peaks are often 100% circularly polarized, with unresolved flares with polarizations of opposite signs sometimes being present in a single subpulse [17–19].

3. OBSERVATIONS AND REDUCTION

The observations of the pulsar B0531+21 whose analysis is considered here were carried out on January 10–11, 2015 from 22:00 to 04:00 UT (the experiment code was RAGS10A). The space radio telescope of the RadioAstron project participated in these observations together with the Westerbork (WB), Arecibo (AR), Effelsberg (EF), and Hartebeesthoek

(HH) ground antennas. The central frequency of the receiver bandwidth was 1668 MHz, with the upper and lower sidebands recorded simultaneously, each with a width of 16 MHz, in two polarization channels: left and right circular polarization (LCP and RCP, respectively). The data were recorded in scans of duration 1170 s, separated by 30-s gaps. At the ground radio telescopes, the data were recorded in MARK5B format with two-bit digitization. We analyzed data for three ground telescopes in our current study: Westerbork (WB), Arecibo (AR), and Effelsberg (EF). These data were played back using the mark5access library for reading MARKIV- and MARK5B-format data developed by Walter Brisken. The analysis of all the data, including the correlation on the ground–space baselines, will be considered in a separate paper. This standard analysis was carried out on the software correlator of the Astro Space Center (ASC) of the Lebedev Physical Institute using specially developed subroutines [11].

We applied the method of coherent dispersion compensation [20] at each radio telescope in our reduction before computing the visibility functions for individual giant pulses. This method can be used to reconstruct the fine structure of the giant pulses, i.e., to obtain the profile of an individual pulse, while the ASC correlator produced the autocorrelation and cross-correlation spectra. We adopted the value $DM = 56.772 \text{ pc/cm}^3$ for the dispersion measure, based on observations carried out at the Jodrell Bank Observatory;¹ the smearing of the pulse in a 16-MHz band is $1773 \mu\text{s}$. For convenience in reading the data, the duration of the “window” for reconstructing the signal was chosen to be two-thirds of the pulse period ($N = 762\,432$ points), so that this mixed the main pulse and interpulse. This window was shifted synchronously with the period; the TEMPO2 program [22] and data from the Jodrell Bank catalog were used for the ephemerides of the pulse arrival times.

Taking into account the contribution of the Crab Nebula, the equivalent system temperatures of the WB, AR, and EF radio telescope were 165, 275, and 900 Jy, respectively. The beam of the Westerbork Synthesis Radio Telescope suppresses the powerful radio emission from the Crab Nebula itself, which has a flux density of 830 Jy at 1668 MHz [23], most efficiently. Therefore, we used recordings from this telescope to directly detect the giant pulses. The detection threshold was at the level 22σ , which corresponded to 3600 Jy. Thus, two types of signal were formed after the dispersion compensation: a detected signal (the power) and an analytical signal (the field). Further, the condition that the signal

¹ <http://www.jb.man.ac.uk/~pulsar/crab.html>

exceed the detection threshold for the WB telescope was verified in each power channel, and the complex cross-correlation functions (CCFs) between the reconstructed analytical signals on the WB–AR and WB–EF baselines—the visibility functions—were calculated when the detection threshold was exceeded. The correlation window had 2048 channels ($\pm 32 \mu\text{s}$), enabling an analysis of the behavior of the amplitude and phase of the visibility function both near its maximum and in its broad wings. The reduction time for a single 20-minute scan, a single baseline combination, and a single polarization channel with coherent dispersion compensation was about 20 hrs on a personal computer. We present here the results of our analysis of observations obtained from 01 : 20 to 04 : 00 UT, when the Arecibo radio telescope was operating. In all, we detected about 1500 giant pulses during this period (2 hrs, 40 min).

4. MEASUREMENT OF THE SCATTERING PARAMETERS

One of the most important scattering parameters is the decorrelation bandwidth of the diffractive spectral distortions. The decorrelation bandwidth can be characterized by the half-width of the autocorrelation function (ACF) of the power spectrum of the signal. For this value to be statistical significant, it must be determined in an interval appreciably exceeding the characteristic scintillation time t_{scint} . It is convenient to express this definition in terms of the dynamical spectrum of the scintillations $F(\nu, t)$ by computing the two-dimensional autocorrelation function, $ACF(\Delta\nu, \Delta t)$, and then analyzing sections of this function. To exclude the influence of noise near zero shifts of $ACF(\Delta\nu, \Delta t)$ in the case of single-telescope data, the CCF obtained for spectra corresponding to the polarizations in the LCP and RCP channels of the telescope is analyzed instead of the ACF.

In the case of VLBI observations, we can also analyze the CCFs obtained for the various radio telescopes participating in the observations. In observations of giant pulses, it is not possible to construct the true dynamical spectrum, since these pulses arrive randomly in time, and the interval between neighboring detected pulses often exceeds the characteristic scintillation time. ACFs obtained for individual spectra are then used to determine the decorrelation bandwidth, via averaging of these ACFs. Here also, the CCFs between spectra obtained for the different polarization channels for a single telescope, or in a single polarization channel for different telescopes, can be used instead of ACFs. The characteristic scintillation time remains outside the framework of our current study in this case.

Figure 1a presents two CCFs, one of which was obtained between spectra in different polarizations for

the Westerbork radio telescope (x's) and the other between spectra obtained in a single polarization (LCP) for two different radio telescopes (Westerbork and Arecibo, circles). There is a large difference between the two functions: the CCF between the different telescopes exceeds the CCF between the different polarization channels by nearly a factor of five, and has a narrow spectral component with a half-width of 50 kHz. At the same time, the CCF between the different polarization channels can be fit well using a single exponential function with a half-width of 320 kHz. This same function is suitable for fitting large frequency shifts of the CCF between telescopes. This same contradiction was obtained earlier by Kondratiev et al. [24] in their analysis of VLBI observations of giant pulses of the Crab Nebula pulsar at 2300 MHz for the Algonquin and Kalyazin telescopes.

Another important scattering characteristic that can be obtained from VLBI observations of giant pulses is the shape and structure of the visibility function $C(\tau)$, which is obtained via an inverse Fourier transform of the cross-spectra signals detected at different radio telescopes in the same polarization channels. Figure 1b shows the mean visibility function $\langle C(\tau) \rangle$ obtained for the baseline between the Westerbork and Arecibo telescopes via averaging all the visibility functions $C(\tau)$ in the upper and lower sidebands of the receiver over 2 hours and 40 minutes of observations. In all, 3600 giant pulses were averaged. The mean visibility function has a narrow peak at zero delay with width $\tau_0 = 1/B$, and has two exponential scales (fitted by a sum of two exponential functions) with half-widths $\tau_1 = 0.10 \mu\text{s}$ and $\tau_2 = 1.0 \mu\text{s}$. The ratio of the amplitudes of the short-time-scale and long-time-scale components is $a_1/a_2 = 3.0$. The central peak in the visibility function shows that the scattering disk was not resolved on the Westerbork–Arecibo baseline (with a projected baseline length of about 6000 km). An important question is which of the two exponential scales should be adopted for the characteristic scattering time τ_{sc} . This quantity plays an important role in estimating the distance to the effective scattering screen. We will return to this question during our discussion of the results of numerical modeling of the scattering.

5. MODELING OF THE SCATTERING

We carried out modeling of the propagation of giant pulses with a specified structure through a scattering medium with a characteristic decorrelation bandwidth. This makes it possible to consider the influence of the characteristic structure of the giant pulses on measurements of the decorrelation bandwidth and the structure of the visibility function.

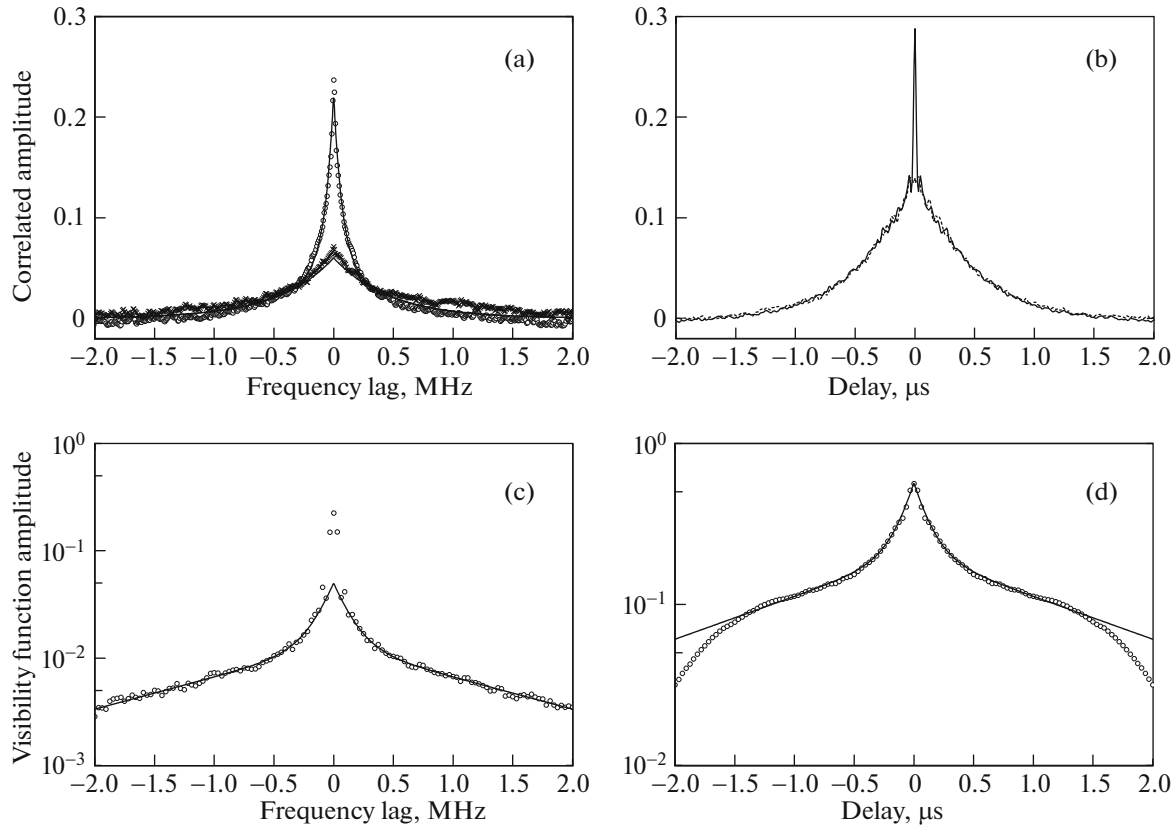


Fig. 1. (a) Cross-correlation functions of spectra. The crosses show the CCF obtained between the autospectra in the RCP and LCP channels for the Westerbork telescope. The circles show the CCF obtained between the autospectra in LCP for the Westerbork and Arecibo radio telescopes. The solid curve shows a fit using two exponentials and the dashed curve a fit with one exponential. (b) Mean amplitude of the visibility function for the Westerbork–Arecibo baseline. The number of averaged giant pulses is $N = 3600$. (c) CCFs obtained by modeling the spectra of the giant pulses. The solid curve corresponds to the CCF between the synthesized spectra for different telescopes in a single polarization. (d) Mean visibility function obtained by modeling the giant pulses. The solid curve corresponds to the sum of two exponential functions with half-widths of 0.09 and 1.12 μs .

We represented the scattering transfer function in the form $K(i\omega) = K(\omega)e^{i\phi(\omega)}$, where $K(\omega)$ is the amplitude response function (ARF) and $\phi(\omega)$ the phase response function (PRF) of the medium. In the theory of linear electric circuits, there is a one-to-one relationship between the ARF and PRF. We can write the transfer function on a logarithmic scale $\ln K(i\omega) = \ln K(\omega) + i\phi(\omega) = A(\omega) + i\phi(\omega)$. As has been shown, for example, by Gonorovskii [25],

$$A(\omega_1) = -\frac{1}{\pi} \int_{-\infty}^{+\infty} \frac{\varphi(\omega)}{\omega - \omega_1} d\omega, \quad (1)$$

$$\varphi(\omega_1) = \frac{1}{\pi} \int_{-\infty}^{+\infty} \frac{A(\omega)}{\omega - \omega_1} d\omega. \quad (2)$$

We can see from these expressions that $A(\omega)$ and $\varphi(\omega)$ are uniquely related via a Hilbert transform, in other words, they are conjugate Hilbert functions.

One of the properties of a Hilbert transform is a simple relationship between the harmonics of the spectra of the conjugate functions, namely, the phases of corresponding harmonics differ by $\pi/2$. This provides a simple means to make a transition from one function to its conjugate. Suppose that the function $A(\omega)$ is known; we can then obtain the Fourier transform of this function and introduce a phase shift between harmonics of $\pi/2$. Essentially, the real and imaginary parts are exchanged. The inverse Fourier transform then gives the function $\varphi(\omega)$.

The structure of the giant pulses was modeled as a random set of unresolved bursts that were equally distributed in an interval of 2 μs with amplitudes having a Gaussian distribution. Each burst was represented as two readings with equal amplitudes and opposite signs. In most of the examples presented below, the number of bursts was taken to be 20. We added a specified level of normally distributed random noise to this structure, such that the signal-to-noise ratio

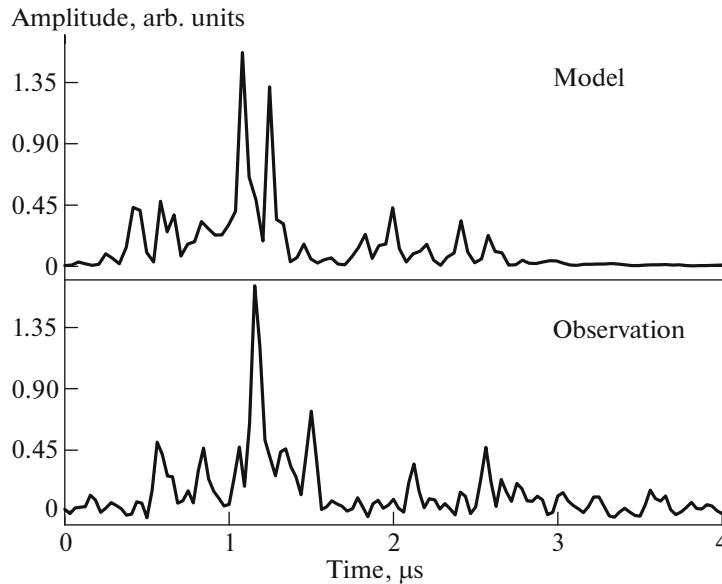


Fig. 2. Temporal structure of individual giant pulses generated by the modeling (upper) and actually observed (lower).

was about 100. Figure 2 shows profiles of individual giant pulses, one of which was generated by the modeling and the other of which was actually observed.

The ARF of the receiver $F(\nu)$ was formed in a band with width $B = 16$ MHz, and specified to have a flat section from ν_b to $B - \nu_b$ and edges that fell off according to the power law $F(\nu) \propto F(\nu - \nu_b)^{-k}$ with $k = 4$. The flat section occupied 0.75 of the entire bandwidth, i.e., 12 MHz. This ARF was superposed on the scintillation spectrum, specified as a sum of two-sided exponential functions $Y_i(\omega) = A_i e^{-b(\omega - \omega_i)}$, whose frequency centers ω_i were randomly and uniformly distributed through the entire receiver bandwidth and whose amplitudes had a Gaussian distribution. The exponential parameter b was chosen in accordance with real measured mean values of the decorrelation bandwidth (about 300 kHz). The number of scintillation peaks in the spectrum was taken to be 10. Further, for each case, the ARF formed was used to compute the PRF as described above, and the result of passing the modeled giant pulse through a specified realization of a scattering medium was obtained by multiplying the spectra of the pulse by the transfer function $K(i\omega)$. This yielded the complex spectrum of the generated signal of a giant pulse that has passed through the specified realization of a scattering medium, which served as the basis for our subsequent comparative analysis.

6. INFLUENCE ON THE DECORRELATION BANDWIDTH

In the subsequent modeling, the decorrelation bandwidth was computed in two ways: by correlating

the spectra obtained for the different polarization channels, and by correlating the spectra obtained in a single polarization channel on different radio telescopes. Recall that different pulse structures are observed in different polarization channels in the case of real giant pulses from the pulsar B0531+21. When modeling using the former approach, we specified different structures of the giant pulses and used the same scintillation structure for both polarizations. When modeling using the latter approach, both the structure of the pulse and the structure of the spectra were the same, and only their noise levels differed.

In all, we generated 10 000 realizations. Figure 1c presents the results of our modeling: the solid curve corresponds to the CCF between the synthesized spectra for the different telescopes in a single polarization (same pulse structure), and the dotted curve the mean CCF between the polarization channels (different pulse structures). The modeled functions confirm the main property of real CCFs (see Fig. 1a), namely, the CCF spectra in a single polarization have an amplitude at zero shift that is a factor of two higher and display a narrow frequency structure at zero shift, while the two functions coincide at large frequency shifts, where they display a purely exponential fall-off with the exponential index specified in the modeling. Thus, the narrow central component is due to the influence of the spectrum of the individual pulses, while the broad component corresponds to the scintillation spectrum. It is therefore this broad component that should be used to determine the decorrelation bandwidth.

7. INFLUENCE ON THE VISIBILITY FUNCTION

We also modeled the visibility functions by correlating the analytical signals for the same structure of the generated pulses passed through the same structure of the scintillation spectra, but with different amounts of white noise added (an interferometer with zero baseline). The mean visibility function for the 10 000 realizations is shown in Fig. 1d. The solid curve passing through the circles represents the sum of two exponential functions with half-widths of 0.09 and 1.12 μs . Only one scale was specified in the modeling, related to the width of the exponential diffractive distortions of the radio spectrum ($\Delta\nu_{1/2} = 300$ kHz). The appearance of an additional short time scale in the mean visibility function is due to the influence of the structure of the individual giant pulses. The absence of a central peak in the modeled mean visibility function is due to the absence of the extended component that is observed in real giant pulses in our model.

Figure 3 compares modeled and observed visibility functions for individual giant pulses. This comparison shows that the passage of pulses consisting of a small number of random unresolved components through a medium giving random distortions with a characteristic frequency scale in the spectrum leads to the appearance of quasi-ordered structures in the visibility function. The appearance of these structures confirms our model for the giant pulses, in which unresolved components dominate and the observed structures are the result of interference between separate, identical wave packets. The time scale for these unresolved components is ≤ 30 ns. In this case, we can estimate a lower limit for the brightness temperature of the giant pulses of the pulsar B0531+21 [26]:

$$T_b \geq \frac{E_p L^2}{k\nu^2 \tau_{GP}^3}, \quad (3)$$

where $k = 1.38 \times 10^{-16}$ erg/K is Boltzmann's constant, ν is the observing frequency, and $\tau_{GP} = 30$ ns is the time scale for an unresolved component of a giant pulse. For the strongest pulse detected in the observations of January 10–11, 2015, $E_p = 3 \times 10^{-26}$ erg/s cm² Hz, yielding the estimated brightness temperature limit $T_b \geq 10^{38}$ K. Other estimates yield similar brightness temperatures [18, 24].

8. A GIANT PULSE AS A STRONG ELECTROMAGNETIC WAVE

How appropriate is the name ‘‘giant pulse’’? Does this phenomenon represent something extraordinary in a physical sense? To answer these questions, we must estimate the strengths of the fields comprising

the electromagnetic wave associated with a giant pulse, in order to compare these with the conditions in the pulsar magnetosphere. The peak flux density of a giant pulse measured in Jy registered by telescopes near the Earth are related to the amplitude of the associated wave by the electro-dynamical relations

$$U = \frac{E^2 + H^2}{8\pi} \equiv \frac{A^2}{4\pi} c \quad (4)$$

$$= S_{\text{peak(Jy)}} \times 10^{-23} \cdot \Delta\nu,$$

where 1 Jy = 10^{-26} W/m² Hz = 10^{-23} erg/s cm² Hz, U is the energy density, E and H are the electric and magnetic field strengths, A is the wave amplitude, which is identically equal to the amplitude of the oscillations of the magnetic or electric field (for an electromagnetic wave, $E = H = A$), $\Delta\nu$ is the frequency bandwidth of the radiation, and c is the speed of light. It follows that the amplitude near the Earth is

$$A_{\oplus} = \left(\sqrt{\frac{4\pi}{c} S_{\text{peak(Jy)}} \Delta\nu} \right) \times 3.3 \times 10^{-12} \quad (5)$$

$$\approx 6.8 \times 10^{-17} \cdot \sqrt{S_{\text{peak(Jy)}} \Delta\nu},$$

Apart from the brightness of the pulse, the observed flux density of a pulse also depends on the parameters of the receiver, most importantly the receiver bandwidth and time resolution. For this reason, the pulse energy E in units of Jy/ μs is often used in place of the flux density. This makes it easy to compare different observations. In this case, $A_{\oplus} = 6.8 \times 10^{-17} \cdot \sqrt{E \Delta\nu / \Delta t}$, where Δt is the pulse duration.

The wave amplitude can conveniently be expressed in units having the dimensions of angular frequency [13], using an expression analogous to the expression for the Larmor gyrofrequency, where the wave field strength is used in place of the constant magnetic-field strength: $\omega_W = eA/mc = 1.76 \times 10^7 \cdot A$. At the boundary of the magnetosphere, in the region of the light cylinder, the flux is $S_{LC} = S_{\text{peak(Jy)}} \cdot (L/R_{LC})^2$. We obtain the corresponding amplitude $A_{LC} = A_{\oplus} \frac{L}{R_{LC}}$ (an inverse square law), where L is the distance from the observer to the pulsar, $R_{LC} = cP/2\pi$ is the radius of the light cylinder, and P is the pulsar period. For the Crab Nebula pulsar, $L = 2$ kpc = 6×10^{21} cm and $R_{LC} = 1.6 \times 10^9$ cm. In this case, $A_{LC} = 3.8 \times 10^{12} \cdot A_{\oplus} = 2.6 \times 10^{-4} \cdot \sqrt{S_{\text{peak(Jy)}} \Delta\nu}$.

The peak flux densities of the giant pulses observed in the Crab Nebula lie in the range 4×10^3 – 10^6 Jy. We derived an estimate for the frequency bandwidth used in our observations, $\Delta\nu = 16$ MHz. In this case,

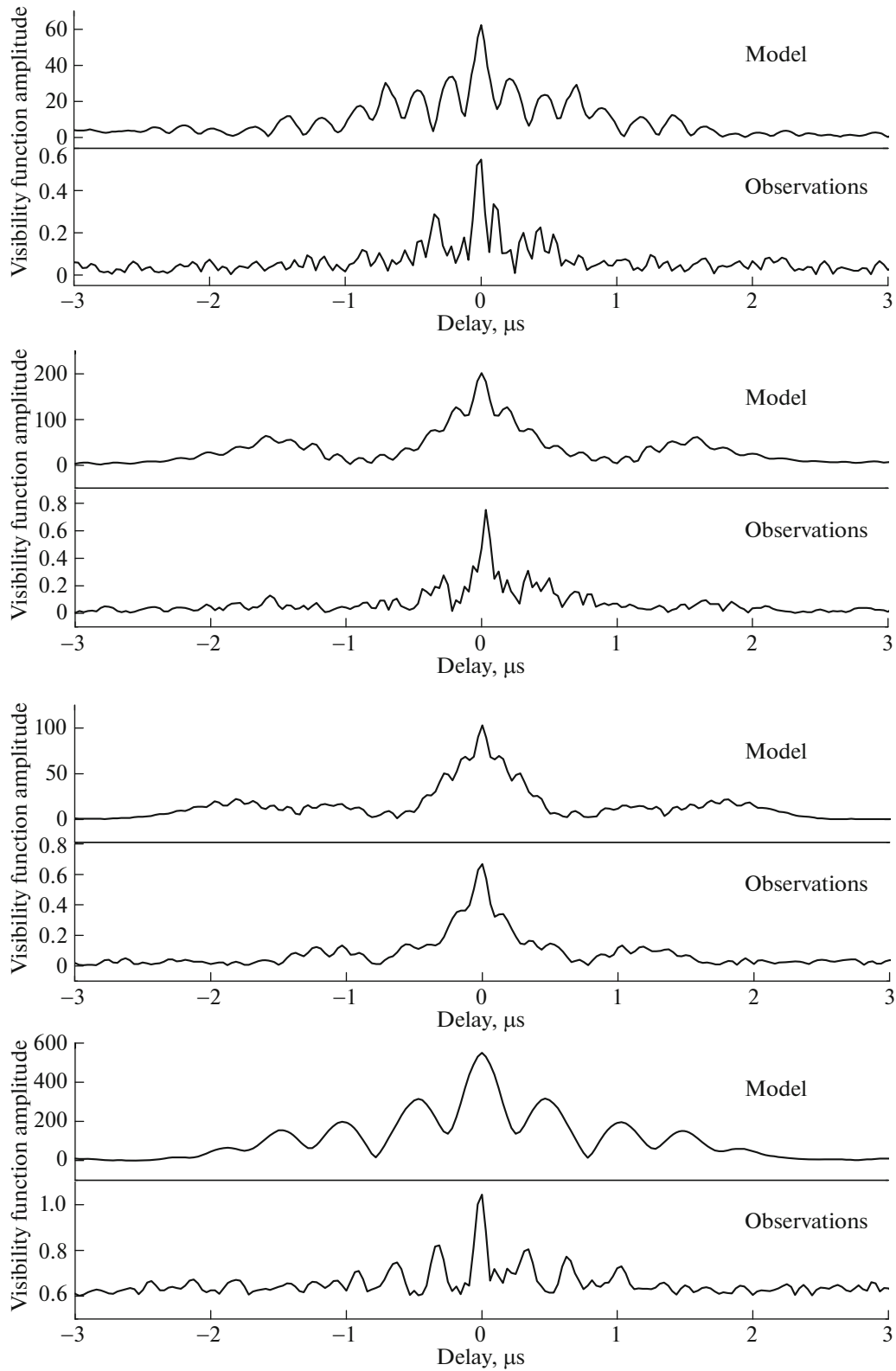


Fig. 3. Four pairs of modeled and observed visibility functions for individual giant pulses. In each pair, the upper and lower curves show the amplitudes of the visibility functions for the modeled and observed pulses, respectively.

the wave amplitude (field strength) of a giant pulse at the light cylinder will be 120–2000 G. These values should most likely be regarded as lower limits, since, as was shown in the previous section (see also [18]), giant pulses are dominated by unresolved components for which $\Delta\nu \sim \nu$. Also, the peak flux density in this case should be increased by a factor of $\nu/16$ MHz compared to the observed value. For a frequency of 1.6 GHz, at which most of our observations have been carried out, this yields $A \sim 3 \times 10^3$.

We also apply the inverse-square law in the region inside the magnetosphere, nearly to the surface of the neutron star, whose radius is $R_* \sim 10^6$ cm. The amplitude of the giant-pulse wave near the surface can be estimated as $A_* = 3 \times 10^{15} \cdot A_{\oplus} = 0.2 \sqrt{S_{\text{peak(Jy)}} \Delta\nu} \sim 5 \times 10^6 - 10^{10}$ G, which corresponds to an energy density $3 \times 10^{12} - 10^{21}$ erg cm $^{-3}$. However, the energy density of the particles carried from the surface and accelerated by the induced electric field fundamentally cannot exceed a fraction $(2\pi R_*/cP)^2 = 4 \times 10^{-5}$ of the energy density of the magnetic field, which is 10^{19} erg cm $^{-3}$. The circumstance that the energy density of the giant pulses exceeds the energy density of the plasma, as was noted in [18], creates great difficulties for attempts to explain such pulses using conventional plasma mechanisms. But another fact is even more important, namely, a more careful analysis leads to the unexpected conclusion that the behavior of electromagnetic waves with amplitudes as high as those observed for giant pulses cannot be described using the usual laws of plasma physics, since these cease to be valid for waves that are strong enough to accelerate charged particles to relativistic speeds.

An obvious criterion for a strong wave is the condition $\omega_W > \omega$, where ω_W is the amplitude of the strong wave in units of angular frequency and ω is the angular frequency of the primary wave. In other words, when $\omega_W/\omega \gg 1$, the wave is strong, and the wave can be considered weak when $\omega_W/\omega \ll 1$. In this case, the character of the interaction between the wave and plasma changes radically: particles radiate in a narrow cone along their motion, primarily in the direction perpendicular to the direction of the primary wave and at higher frequencies. There is no interference between secondary and primary waves, and interactions between particles and waves reduce to a loss of the energy of the wave to acceleration of the particles; in other words, giant pulses act like efficient particle accelerators.

The problem of the motion of a charged particle in the field of an electromagnetic wave has an exact analytical solution that is valid for any value of ω_W/ω [27]. It follows that, if $\omega_W \gg \omega$, in the field of a circularly polarized wave, a particle moves in a circle

with radius $\lambda/2\pi$ (λ is the wavelength), in a plane that is perpendicular to the direction of propagation of the primary wave, with Lorentz factor $\gamma = \omega_W/\omega$, and radiates at the frequency $\omega_{em} \sim \omega\gamma^3 = \omega_W^3/\omega \gg \omega$ within the opening angle $\theta_{em} \sim \gamma^{-1} \approx \omega_W/\omega$ —a full analog of synchrotron radiation. In the field of a linearly polarized wave, the particle will move along a trajectory having the shape of a figure eight in the plane of \mathbf{E} and the wave vector \mathbf{k} . The longitudinal axis of the figure eight is perpendicular to the direction of propagation of the wave. The Lorentz factor varies along the trajectory from $\gamma = 0.36\omega_W$ at the edges to $\gamma = 1.03\omega_W/\omega$ at the center.

Possible evidence for such “side” emission may be provided by the extreme variations in the pulsar profile at frequencies above 4 GHz [15]. The main pulse disappears completely, and the phase of the interpulse jumps by 15° . Two broad features appear at longitudes where there was no emission at all at lower frequencies. We suggest that this behavior can be interpreted as radiation from particles accelerated in the wave field associated with the giant pulses. We intend to consider this question in more detail in subsequent studies.

With regard to the nature of giant pulses and their role in the formation of the emission of a pulsar, we suggest a scenario in which giant pulses are born near the surface of the neutron star during a cascade breakdown of the vacuum gap, as a natural consequence of the appearance of volume charge, which accompanies this process. The giant pulse then acts like an efficient particle accelerator along the entire path from the neutron-star surface to the boundary of the magnetosphere. The Crab Nebula pulsar is a young object with a short period and accordingly a small radius for the light cylinder. Therefore, a giant pulse is able to spend only a small fraction of its energy on particle acceleration during the short time required for its passage through the magnetosphere. Old pulsars with periods of order a second have magnetospheres a factor of ten larger, so that all the energy in giant pulses goes into particle acceleration. In this latter case, a pulse expends all its energy, but excites the plasma of the magnetosphere in the process, making possible the generation of radio emission via standard plasma mechanisms (for example, as a result of two-stream instability).

9. CONCLUSION

Our modeling of the influence of scattering on the scattering parameters (the decorrelation bandwidth and the characteristic scattering time) has enabled us to draw the following conclusions.

In addition to diffractive distortion, a narrow-band feature due to the spectrum of the giant pulse itself

appears in the power spectrum of the signal from a giant pulse. The broadband feature in the CCF of the autospectra obtained on different radio telescopes should be adopted as the measured decorrelation bandwidth.

An additional short-scale feature associated with fine structure of the giant pulses themselves also appears in the mean visibility function. Here, too, the characteristic scattering time is indicated by the extended component of the mean visibility function.

The observed quasi-regular visibility functions of individual giant pulses indicate the presence of strong, unresolved components in the structure of these pulses at 1668 MHz. Similar components were observed earlier only at frequencies above 5 GHz, in the frequency range where they are not blurred by scattering. Thus, VLBI observations of giant pulses from the Crab Nebula pulsar indicate the presence of fine structure in the pulses at 1668 MHz—unresolved peaks with durations $\tau \leq 30$ ns and brightness temperatures $T_b \geq 10^{38}$ K. Taking into account the discussion in the previous section, we conclude that unresolved components with such high brightness temperatures will propagate as strong electromagnetic waves that accelerate particles in the ambient plasma. This gives rise to new components in the pulsar pulse profile (HFC1, HFC2) at frequencies above 4 GHz [15].

ACKNOWLEDGMENTS

This work was supported by a grant from the Presidium of the Russian Academy of Sciences (Program No. 7). The RadioAstron project has been realized by the AstroSpace Center of the P.N. Lebedev Physical Institute of the Russian Academy of Sciences and the S.A. Lavochkin Scientific Production Association, by contract with the Russian Space Agency, jointly with many scientific and technical organizations in Russia and other countries. The results presented are partially based on observations carried out on radio telescopes of the Institute of Applied Physics of the Russian Academy of Sciences.

REFERENCES

1. J. H. Taylor and J. M. Cordes, *Astrophys. J.* **441**, 674 (1993).
2. T. H. Hankins and B. J. Rickett, *Methods Comput. Phys.* **14**, 55 (1975).
3. P. A. G. Scheuer, *Nature* **218**, 920 (1968).
4. B. J. Rickett, *Ann. Rev. Astron. Astrophys.* **15**, 479 (1977).
5. A. G. Lyne and D. J. Thorne, *Mon. Not. R. Astron. Soc.* **172**, 97 (1975).
6. C. R. Gwinn, M. C. Britton, J. E. Reynolds, D. L. Jauncey, E. A. King, P. M. McCulloch, J. E. J. Lovell, and R. A. Preston, *Astrophys. J.* **505**, 928 (1998).
7. C. R. Gwinn, N. Bartel, and J. M. Cordes, *Astrophys. J.* **410**, 673 (1993).
8. N. S. Kardashev, V. V. Khartov, V. V. Abramov, V. Yu. Avdeev, A. V. Alakoz, et al., *Astron. Rep.* **57**, 153 (2013).
9. M. V. Popov, A. S. Andrianov, N. Bartel, C. R. Gwinn, M. D. Johnson, B. C. Joshi, N. S. Kardashev, R. Karuppusamy, Y. Y. Kovalev, M. Kramer, A. G. Rudnitskii, E. R. Safutdinov, V. I. Shishov, T. V. Smirnova, V. A. Soglasnov, et al., *Astrophys. J.* **822** (2) 2016.
10. M. V. Popov, A. S. Andrianov, N. Bartel', K. Gwinn, B. Ch. Dzhoshi, N. S. Kardashev, A. G. Rudnitskii, T. V. Smirnova, V. A. Soglasnov, E. N. Fadeev, and V. I. Shishov, *Astron. Rep.* **93** (9), 778–794 (2016).
11. A. G. Rudnitskii, R. Karuppusami, M. V. Popov, and V. A. Soglasnov, *Astron. Rep.* **60**, 211 (2016).
12. J. M. Cordes, N. D. R. Bhat, T. H. Hankins, M. A. McLaughlin, and J. Kern, *Astrophys. J.* **612**, 375 (2004).
13. V. A. Soglasnov, in *Neutron Stars and Pulsars: 40 Years after the Discovery*, Ed. by W. Becker and H. H. Huang (2007), p. 68.
14. M. V. Popov and B. Stappers, *Astron. Astrophys.* **470**, 1003 (2007).
15. T. H. Hankins, G. Jones, and J. A. Eilek, *Astrophys. J.* **802**, 130 (2015).
16. B. J. Rickett, *Astrophys. J.* **197**, 185 (1975).
17. T. H. Hankins and J. A. Eilek, *Astrophys. J.* **670**, 693 (2007).
18. T. H. Hankins, J. S. Kern, J. C. Weatherall, and J. A. Eilek, *Nature* **422**, 141 (2003).
19. M. V. Popov, V. A. Soglasnov, V. I. Kondrat'ev, A. V. Bilous, S. V. Sazankov, A. I. Smirnov, B. Z. Kanevskii, V. V. Oreshko, and Yu. P. Ilyasov, *Astron. Rep.* **52**, 900 (2008).
20. T. H. Hankins, *Astron. Astrophys. Suppl.* **15**, 363 (1974).
21. A. G. Lyne, R. S. Pritchard, and F. Graham-Smith, *Mon. Not. R. Astron. Soc.* **265**, 1003 (1993).
22. G. B. Hobbs, R. T. Edwards, and R. N. Manchester, *Mon. Not. R. Astron. Soc.* **369**, 655 (2006).
23. M. F. Bietenholz, N. Kassim, D. A. Frail, R. A. Perley, W. C. Erickson, and A. R. Hajian, *Astrophys. J.* **490**, 291 (1997).
24. V. I. Kondratiev, M. V. Popov, V. A. Soglasnov, Y. Y. Kovalev, N. Bartel, W. Cannon, and A. Y. Novikov, *Astron. Astrophys. Trans.* **26**, 585 (2007).
25. I. S. Gonorovskii, *Radio Technical Circuits and Signals. Textbook for Higher Education* (Radio Svyaz', Moscow, 1986) [in Russian].
26. V. A. Soglasnov, M. V. Popov, N. Bartel, W. Cannon, A. Yu. Novikov, V. I. Kondratiev, and V. I. Altunin, *Astrophys. J.* **616**, 439 (2004).
27. L. D. Landau, E. M. Lifshits, *Course of Theoretical Physics, Vol. 2: The Classical Theory of Fields* (Nauka, Moscow, 1988; Pergamon, Oxford, 1975), Chap. 6.

Translated by D. Gabuzda